A review of optical near-fields in particle/tip-assisted laser nanofabrication

Z B Wang[1*], **N Joseph**[1], **L Li**[1], and **B S Luk'yanchuk**[2]

[1]Laser Processing Research Center, School of Mechanical, Aerospace, and Civil Engineering, University of Manchester, Manchester, UK

[2]Data Storage Institute, DSI Building, Singapore, Republic of Singapore

The manuscript was received on 6 June 2009 and was accepted after revision for publication on 5 October 2009.

DOI: 10.1243/09544062JMES1766

Abstract: Nanofabrication by using lasers with a spatial resolution beyond the optical diffraction limit is a challenging task. One of the solutions is to use near-field techniques, in which evanescent waves dominate over free waves in the vicinity of scattering objects and sub-diffraction-limited focus (as small as ~10 nm) can be achieved. Theoretical modelling of near-field phenomena is extremely important for the understanding of these near-field techniques, especially for some cases where it is not possible to directly measure the near-fields. In this article, a brief review of the existing near-field laser nanofabrication techniques is given. Different theoretical methods for the computation of optical near-fields, including both analytical and numerical methods, are then presented. The optical near-field distributions of different micro/nano-systems (isolated particles, aggregated particles, particles on the substrate, particles in liquid, and the tip-sample system) are then reviewed in detail within the framework of laser nanofabrication.

Keywords: laser nanofabrication, near-field, evanescent wave, diffraction limit

1 INTRODUCTION

Laser nanofabrication has become increasingly important due to the rapid development of nanophotonics, super-resolution optical lithography, ultrahigh density optical data storage, and biomedical devices [**1**]. In laser nanofabrication, the pattern resolution is normally determined by the minimum spot size of the laser beam at focus. In the cases where the laser focus is in the far-field zone of the focusing elements, the optical diffraction limit imposes that light cannot be confined to a lateral dimension Δx smaller than roughly one half of the wavelength λ in free space [**2**].

The physical nature of the diffraction limit is related to the free propagation waves in the far-field zone. Free propagation is characterized by a $\boldsymbol{k}$-vector whose three components all are real values. Therefore, none of the components (k_x, k_y, k_z) can be larger than k_i as $k_i^2 = k_x^2 + k_y^2 + k_z^2$. In order to overcome the diffraction limit for super-resolution nanofabrication, near-field optics (NFO) has attracted great attention in recent years. NFO deals with optical phenomena where evanescent waves becomes significant over free prorogation waves. Evanescent waves are characterized by a rapid decay of their amplitudes in at least one direction in space. The respective component(s), for example k_z, of the wavevector are imaginary (more generally, complex). The residual components like k_x, hence, can be larger (in fact much larger because of momentum conservation) than $|k_i|$ as $k_i^2 = k_x^2 + k_y^2 + k_z^2$, and Δx can be much smaller than half of the wavelength.

Strong evanescent waves are excited preferentially (although not exclusively) at the boundary of two different media, for example by total internal reflection (TIR), light interaction with sub-wavelength period gratings or small micro/nano-objects (particles, tips, apertures, etc.) whose sizes are comparable to the incident wavelength. Evanescent waves are undamped electromagnetic modes at two *dielectric* media interfaces. Unlike dielectrics, the free electron gas of metals can sustain surface and volume charge density oscillations (i.e. plasmonic resonance wave, leading to the absorption and scattering of laser light in

*Corresponding author: *Laser Processing Research Center, School of Mechanical, Aerospace, and Civil Engineering, University of Manchester, P.O. Box 88, Sackville Street, Manchester, Lancashire, M60 1QD, UK.*

email: zengbo.wang@manchester.ac.uk

an unusual way compared to dielectrics [**3**]). The plasmonic waves are damping electromagnetic modes due to the high dissipative factor of metals and can only propagate a limited short distance (typically several tens of micrometers) along the surface. Despite the slightly different physical natures of evanescent waves and plasmonic waves, both waves are near-field limited and are able to confine light into a sub-diffraction-limited spot, which is important for laser nanofabrication.

In reality, surface nanostructures can be created by either optical lithography of photosensitive materials or direct patterning on a substrate surface. For the surface nanostructuring in industries, many efforts are required to develop novel high-throughput, high-resolution, and low-cost nanofabrication techniques. The existing near-field laser nanofabrication techniques include the following sub-sections.

1.1 Particle-lens array

The particle-lens array (PLA) technique employs a regular two-dimensional (2D) array of small particles as a lens array, which converts a laser beam into a multiplicity of enhanced optical spots in parallel at focus in near-field. Its efficiency is extremely high and millions or billions of nanostructures can be fabricated with a single laser pulse irradiation once the sample is prepared, making it ideal for large-area surface nanofabrication [**4**, **5**]. PLA utilizes the near-field focusing effect of transparent or plasmonic micro-sized particles induced by optical resonances. Unlike the micro-lens array system that forms an array of foci in the far-field, the near-field foci in the PLA system allow for better focusing for a smaller spot size and higher field enhancement. It has been demonstrated that PLA can be combined with an angular scanning laser beam for the fabrication of an array of arbitrary-shaped complex nanostructures with a sub-diffraction resolution of 80 nm with a 248 nm laser source [**6**]. Meanwhile, PLA can be completely immersed into liquid solutions during processing, making chemical or biological reactions controllable in the nanoscale [**7**]. Smaller features with a resolution down to 30 nm can be obtained by PLA with 140 nm dielectric particles and a 248 nm laser source [**8**]. In short, PLA is a parallel, low-cost nanofabrication technique and is promising for real industrial applications involving processing of large samples. The main challenge is to form highly ordered self-assembled particles on the sample surface in a short time period.

1.2 Laser-assisted atomic force microscope/ scanning tunnelling microscope tip

A pulsed laser irradiation of the gaps between the atomic force microscope (AFM) tip and the sample surface induces enhanced optical near-fields around the tip, leading to nanostructure formation on the substrate surface that is placed close enough to the tip. Arbitrary-shaped nanopatterns can be fabricated by controlling the scanning path of the tip. The lateral resolution of $\sim$10 nm has been demonstrated in the literature [**9–12**]. The drawback is that it is a serial processing technique and large-area processing is difficult.

1.3 Near-field scanning optical microscope

The near-field scanning optical microscope (NSOM) is the main instrumentation used for the imaging of near-field optical signals with subwavelength resolution. The surface that will be imaged is placed close to the NSOM tip aperture (within nanometres). The resolving power of the NSOM is dependent on the aperture or tip opening size (typically 50 nm and larger) instead of the light wavelength. Unlike in the laser-assisted AFM/scanning tunnelling microscope (STM)-tip laser nanofabrication technique where laser light was coupled to the tip-sample gap from the sides, in NSOM the laser light was guided into the hollow fibre tip and emits through the tip aperture as evanescent waves for surface patterning. Arbitrary-shaped nanopatterns can be fabricated and the pattern resolution down to 25 nm has been demonstrated in the literature [**13–16**].

1.4 Plasmonic lithography

Plasmonic lithography (PL) utilizes the ultrashort wavelength of and field localization of surface plasmon (SP) for nanolithography. The lithography mask generally consists of a silver thin film perforated with 2D hole arrays exhibiting superior confinement due to SPs with a wavelength equal to 1/4 of that of illuminating light (365 nm). Small features with resolution down to 30 nm can be obtained [**17**, **18**]. To fabricate user-defined patterns, photo masks need to be pre-fabricated in the PL technique.

It is worth mentioning that the laser-assisted nanoimprinting technique is also used for nanofabrication. However, the resolution in the nanoimprinting process is determined by mould feature size instead of laser focus size. Laser is used to heat up and soften the substrate surface for a better transfer of pattern from the mould to the substrate during mechanical pressing [**19**]. Other techniques such as laser interference lithography are also mentioned in the literature for nanofabrication, but it is indeed a diffraction-limited technique and high resolution is attained by over-exposure of photoresist material.

It is clear that a theoretical understanding of the optical near-field distributions is of great importance for different near-field laser nanofabrication techniques. Historically, NFO begins with NSOM. The long history of NSOM has helped in producing a large

body of literature addressing the theoretical issue of the system [**1**, **20**–**25**]. The PL technique is mainly propounded by Prof. Zhang's group at UC Berkeley, and the SP polariton theory behind the technique is also well documented [**26**–**32**]. On the other hand, there are fairly limited papers devoted to the theoretical aspects of PLA and laser-assisted AFM/STM-tip techniques. In this article, following a brief introduction of simulation techniques that are suitable for modelling near-field phenomena, the near-field distributions of particle systems (*isolated particles, aggregated particles, particles on the surface,* and *particles in liquid medium*) and tip-sample systems (*dielectrics* or *plasmonic tip and sample*) are reviewed, which has a close connection with PLA and the laser-assisted AFM/STM-tip nanofabrication technique, respectively.

2 THEORETICAL METHODS

Existing theories of electromagnetic waves describe satisfactorily their interaction with objects whose sizes are much larger (theory: the Kirchhoff approximation) or much smaller than (theory: dipole approximation and Rayleigh scattering) the incident wavelength. These approximations, however, are not suitable for the scattering of electromagnetic waves by micro/nano-systems whose sizes are comparable to the incident wavelength (referred to as the mesoscopic system hereinafter). The mesoscopic systems require the detailed solution of the full set of Maxwell equations to modelling the optical near-fields. The main complexity of such modelling can be traced back to the crucial role played by the evanescent components of the field in the near-field zone close to mesoscopic scatterers. In a complete analogy with the tunnel effect for electrons, these evanescent components can lead to optical tunnel effects. The accurate treatment of evanescent waves requires one to deal carefully with the electromagnetic boundary conditions at each interface where evanescent waves could dominate over free waves.

Theoretical methods for the calculation of optical near-fields can be divided into analytical and numerical categories. In this section, the basics, advantages and disadvantages of different analytical and numerical methods that are frequently used for NFO modelling are briefly reviewed.

2.1 Analytical and semi-analytical methods

2.1.1 Mie theory

Small particles in spherical or cylinder shapes are common research objects in nanooptics and NFO. For example, in the PLA laser nanofabrication technique, the laser light was focused by micro/nano-spheres and thus Mie theory plays an important role here. Mie theory was developed a century ago in 1908 and is an exact analytical solution of the Maxwell equation for light scattering by a spherical particle with arbitrary size and refractive index and immersed in an arbitrary surrounding medium. Both near-field information such as intensity distribution and far-field information such as absorption/scattering/extinction efficiencies can be obtained with the theory. Detailed formulations of Mie theory can be found in Stratton [**33**] or Born and Wolf [**34**]. It should be noted that Mie theory was initially developed for isolated homogeneous single particles embedded in a homogeneous surrounding medium so that situations such as particles situated on a surface, non-spherical particles, and aggregated particles cannot be exactly modelled. In these cases, other techniques should be used. Nevertheless, the main field enhancement effect as in the PLA technique can be demonstrated qualitatively with Mie theory and provides valuable information for experimental design and implementation.

There are four key input parameters in Mie theory (i.e. incident laser wavelength, medium refractive index, particle size, and particle refractive index), but they can be reduced to two independent input parameters of (q, n_p), where q is size parameter defined as $q = 2\pi a/\lambda$, and a is the particle radius, λ the laser wavelength, and n_p the particle refractive index.

2.1.2 Extended Mie theory for particles on the surface

As was noted above, Mie theory does not take into account the surface influences on the field distribution. Owing to reflection and secondary scattering of the reflected radiation of the substrate, the final field distribution could be quite different. In the limit of geometrical optics, a well-known effect often named as Newton rings, will arise because of the interference of scattered and reflected radiations. A rigorous analytical solution to the surface problem for such particles was given by Bobbert and Vlieger in 1986 [**35**] (hereafter referred to as the BV theory), and was limited to far-field scattering problems [**36**]. The main governing equation in the BV theory is

$$W^\mathrm{S} = \mathbf{B}(V^\mathrm{I} + V^\mathrm{IR} + V^\mathrm{SR}) \tag{1}$$

where W^S represents the scattering wave, V^I the incidence wave, V^IR the reflected incidence wave, and V^SR the reflected scattering wave. The $\mathbf{B}$ matrix is exactly the same as that in Mie theory. The V^SR wave and the W^S wave are linearly related by a matrix $\mathbf{A}$ that characterizes the reflection of spherical waves by the substrate

$$V^\mathrm{SR} = \mathbf{A}\, W^\mathrm{S} \tag{2}$$

From equations (1) and (2), one can find that the formal solution is

$$W^\mathrm{S} = (1 - \mathbf{B}\,\mathbf{A})^{-1}\mathbf{B}(V^\mathrm{I} + V^\mathrm{IR}) \tag{3}$$

Thus, the technical problem is related to the calculation of the 'scattering reflection matrix' **A** and the inverse matrix $(1 - \mathbf{B}\,\mathbf{A})^{-1}$ in equation (3). The **A** matrix is obtained from the generalization of the Weyl integration method by which the spherical scattering W^{S} wave is expressed as an integral over plane waves travelling in various directions [**35**]

$$A_{l',m',f';l,m,f} = i^{l'-1}\left[\frac{2l'+1}{l'(l'+1)}\right]^{1/2}(-1)^{m-1}\delta_{mm'} \times \int_0^{\pi/2-i\infty} \sin\alpha\, \mathrm{d}\alpha \mathrm{e}^{2iq\cos\alpha} a^m_{l',f';l,f}(\alpha) \quad (4)$$

To extend the BV theory for near-field problems, Wang *et al.* [**5**] proposed that the total field in the optical near field can be calculated by constructing the total Debye potentials as

$${}^{f}D(r,\theta,\phi) = \sum_{l=1}^{\infty}\sum_{m=-l}^{l}\left\{\left[{}^{f}(V_l^m)^{I} + {}^{f}(V_l^m)^{\mathrm{IR}} + {}^{f}(V_l^m)^{\mathrm{SR}}\right] \times j_l(kr) + {}^{f}(W_l^m)^{S} h_l^{(1)}(kr)\right\} Y_l^m(\theta,\phi) \quad (5)$$

where $j_l(kr)$ and $h_l^{(1)}(kr)$ are the spherical Bessel and Hankel functions of order l, respectively. The index f in equation (5) can be $e({}^{e}D)$ or $h({}^{h}D)$, representing the electric Debye potential and the magnetic Debye potential, respectively. An improved algorithm was also given in reference [**5**] to calculate the reflection scattering matrix V^{SR}. Effects of the substrate on the optical near-field, including stronger field enhancement and multiple rings, will be reviewed below in this article.

2.1.3 Multiple multi-pole

The multiple multi-pole (MMP) is a semi-analytical method between a purely analytical approach and a purely numerical approach. It is used for solving Maxwell equations in arbitrarily shaped, isotropic, linear, and piecewise homogeneous media. The method is suited to analysing extended structures since only the boundaries between homogeneous media need to be discretized and not the media themselves. Essentially, the field is expanded by a series of basis fields. Each of the basis field is an analytic solution of the field equations within a homogeneous domain. The amplitudes of the basis fields are computed by a generalized point matching technique that is efficient, accurate, and robust. The MMP technique provides an analytical expression for the solution of the electromagnetic field and also provides a reliable validation of the results, as the errors can be calculated explicitly. More details of the method can be found in reference [**37**].

2.1.4 Volume integral methods

It is known that small particles can often be approximated by dipolar elements as in the case of Rayleigh scattering. The induced dipole moment in such a particle is proportional to the local field at the position of dipole. As long as a single particle is considered, the local field corresponds to the illuminating incident field. However, if an ensemble of particles is considered, the local field is a superposition of the incident radiation and all the partial fields scattered by the surrounding particles. It thus turns out that each particle is dependent on all the other particles. To solve this problem, formalism is needed for solving self-consistent fields of an arbitrary number of particles that interact coherently. The particles are not required to be spatially separated from each other. They can be joined together to form a macroscopic object. Indeed, the response of matter to incident radiation can be formulated as a collective response of individual dipoles each of them occupying a volume element. This superposition of elementary dipole fields (Green's functions) has to be done in a self-consistent way (i.e. the magnitude and the orientation of each individual dipole are a function of the local field defined by the excitation and other surrounding dipoles). Methods based on this concept usually involve summations over all dipolar centres. In the limit, as the size of the dipolar centres goes to zero, the summations become volume integrals. Therefore, these formalisms are denoted as volume integral methods. In both a microscopic and a macroscopic point of view, there exists basically the same formalism. Whereas in the former, microscopic dipolar particles are joined together to form a macroscopic ensemble, the latter considers a macroscopic object that is divided into small homogeneous subunits. One of the methods following the microscopic point of view is the coupled dipole method (CDM), and one of the methods following the macroscopic point of view is the method of moments (MOM). It was shown by Lakhtakia that the two formalisms are physically and mathematically equivalent, with one formalism in a weak form (MOM) and the other in a strong form (CDM) [**38**]. In the literature, CDM is also called discrete dipole approximation and MOM is designated as the digitized Green function method. More details about MOM and CDM can be found in references [**1**], [**39**], and [**40**].

2.2 Pure numerical methods

Popular pure numerical methods for nanooptics and NFO include the finite-element method (FEM) [**41**], the finite-difference time-domain (FDTD) technique [**42**], and the finite integral technique (FIT) [**43**]. These methods can easily handle complex geometries by dividing the structures into small subdomains.

2.2.1 *Finite-element method*

The FEM originated from the need to solve complex elasticity and structural analysis problems in civil and aeronautical engineering and has by now been generalized to almost all science and engineering branches including the nanooptics and NFO topics in the present article. Generally, FEM makes use of a variation formulation (or weak formulation) of the wave equations. In the case of a 2D problem (H_z, E_x, E_y)

$$\int_{\Omega}\left[\nabla\left(\frac{1}{\varepsilon_{\mathrm{r}}}\nabla H_z\right)+\frac{\omega^2}{c^2}H_z\right]v\,\mathrm{d}\Omega=0 \tag{6}$$

where v is the test function defined on domain Ω. The integrals based on weak formulation enable one to consider the domain of computations as a union of N subdomains. The problem is solved on each subdomain and the global solution is then the sum of the solutions for each element. Equation (6) is the projection of the solution on the basis of test functions v. The solution verifies exactly the partial differential equation (PDE) on each node for the given boundary conditions. The basis of polynomial functions v gives an approximation of the solution into the element. Numerical implementation involves a finite basis of functions and, consequently, a linear system is solved by classical numerical LU decomposition or by a bi-conjugate gradient iterative procedure for large systems. The self-adaptive mesh refinement scheme is usually important for accurate FEM modelling [**41**]. FEM is a frequency domain method for the simulation of near-field problems so that arbitrary dielectric constants including the negative dielectric constant for plasmonic micro/nano-structures can be set into program using experimental values.

2.2.2 *Finite difference in time domain*

The FDTD method is a direct space method, first introduced by Yee in 1966 and now widely used for solving electromagnetic problems. It mainly consists of the discretization of curl-Maxwell's equations by iteration over the time. With a spatial discretization Δx and a temporal discretization Δt, one can obtain the standard recursion equations in a non-dispersive and non-magnetic medium for the electric and magnetic fields for a 2D p-polarization incidence wave (H_z, E_x, E_y)

$$\begin{aligned}
H_z|_{i,j}^{n+1/2} &= H_z|_{i,j}^{n-1/2}+\frac{\Delta t}{\mu_0\Delta x}\\
&\quad\times\left(E_x|_{i,j+1}^{n}-E_x|_{i,j}^{n}+E_y|_{i,j}^{n}-E_y|_{i+1,j}^{n}\right)\\
E_x|_{i,j}^{n+1} &= E_x|_{i,j}^{n}+\frac{\Delta t}{\varepsilon_0\varepsilon_{i,j}\Delta x}\left(H_z|_{i,j}^{n+1/2}-H_z|_{i,j-1}^{n+1/2}\right)\\
E_y|_{i,j}^{n+1} &= E_y|_{i,j}^{n}+\frac{\Delta t}{\varepsilon_0\varepsilon_{i,j}\Delta x}\left(H_z|_{i-1,j}^{n+1/2}-H_z|_{i,j}^{n+1/2}\right)
\end{aligned} \tag{7}$$

where ε_0 and μ_0 are the permittivity and permeability of free space, and $\varepsilon_{i,j}$ is the relative permittivity at position $x=i\,\Delta x$, $y=i\,\Delta y$, any field U (either H or E) at position $x=i\,\Delta x$ and for the instant $t=n\,\Delta t$ being represented by $U|_i^n$. The upper limit for Δt is given by the Courant time step $t_{\mathrm{c}}=\Delta x/(c\sqrt{N})$, and N is the dimension of the problem. FDTD is especially useful for the spectroscopic studies since full spectrum results can be obtained in a single run of the program. Unlike in FEM, FDTD is a time domain method and the dielectric constants of the material were usually fitted by different material models such as the Debye or Lorentz or the modified Drude or modified Debye models. Accurate models for material dispersions still remain a challenge in FDTD [**42**].

2.2.3 *Finite integral technique*

The FIT, proposed by Weiland [**43**], provides a universal spatial discretization scheme, applicable to various electromagnetic problems, ranging from static field calculations to high frequency applications in the time or frequency domain. Unlike other numerical methods, FIT discretizes the Maxwell's equation in an integral form rather than the differential ones. In the case of Cartesian grids, the FIT formulation can be rewritten in the time domain to yield standard FDTD methods. While in the case of triangular grids, the FIT has tight links with FEM methods formulated in Whitney forms [**44**]. In a non-strict sense, the FIT technique can be referred to as a hybrid combination of FDTD and FEM techniques. CST Microwave studio software is the leading FIT software in the market [**45**].

3 OPTICAL NEAR-FIELDS IN LASER NANOFABRICATION

In laser nanofabrication, field intensity distribution at the focal region is of particular interests. However, the term 'intensity' is somehow ambiguous in the literature and was used for both the time-averaged Poynting vector ($\bar{\boldsymbol{S}}=1/2\;Re\{\boldsymbol{E}\times\boldsymbol{H}^{\bullet}\}$) and electric field amplitude ($I=\vec{\boldsymbol{E}}\,\boldsymbol{E}^{*}\equiv|\vec{\boldsymbol{E}}|^2$). As will be shown below, the Poynting field intensity is different from the electric field amplitude intensity in optical near-fields. Therefore, it is necessary to identify which intensity is controlling the process by comparing theoretical and experimental results. Depending on the specific process, different field intensity distributions for different micro/nano-systems are presented below.

3.1 Isolated particles

In the limiting cases of geometrical optics and dipole approximation, the field is obtained with approximations. By Mie theory, we are able to see the exact field distribution. An example of Mie calculation is shown in

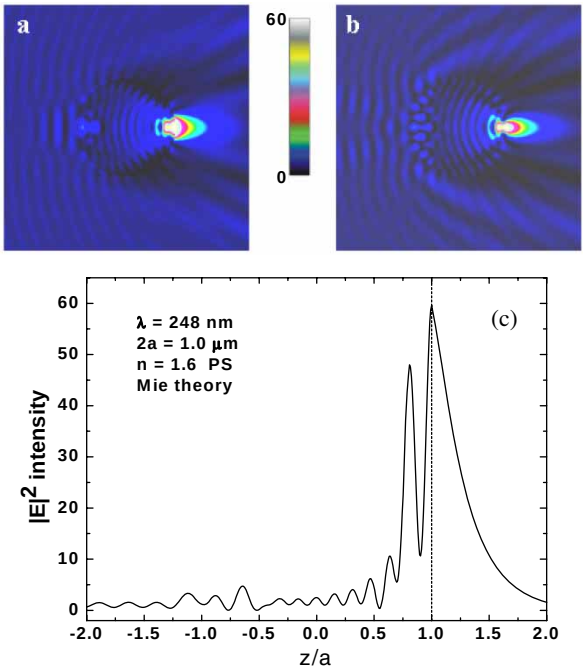

Fig. 1 Spatial intensity distribution, $I = |E|^2$, inside and outside the 1.0 μm PS particles, illuminated by a laser pulse at $\lambda = 248$ nm, and (a) polarization parallel and (b) perpendicular to the image plane. The maximum intensity enhancement in calculations is about 60 for both regions. (c) Intensity along the z-axis. $z = 1.0$ is the position under the particle

Fig. 1 for a 1.0 μm polystyrene (PS) particle illuminated by a laser pulse at $\lambda = 248$ nm.

From Fig. 1, it can see that the electric field is greatly enhanced in the near-field region under the transparent particles. The electric field enhancement decays quickly (almost exponentially as a character of NFO) from 59.6 at $z = a$ to 1.57 at $z = 2a$. Within the $z = a$ tangential plane, the distribution of laser intensity is shown in Fig. 2.

One can see the high localization of laser intensity in this plane. It should be noted the intensity profiles of $I = |E|^2$ and $I = S_z$ shown here are different from each other although the peak values are similar. The profile of the $|E|^2$ intensity is not in a round shape but with a ratio of about 2:1. However, the S_z intensity presents a nearly round focusing. The difference between them originally comes from the contribution of the r-component of the electrical vector $\boldsymbol{E}_r$, which decays with r as $\boldsymbol{E}_r \propto 1/r^2$. This vector quickly tends to zero in the far field ($r \geqslant \lambda$) [**34**]. In other words, the scattered wave in the far field is a transverse wave for which the $|E|^2$ and S_z intensities are identical. But the scattered wave in the near field is not transverse, which results in the difference. In pulsed-laser nanofabrication and cleaning, we are more interested in the S_z field distribution under the particles. It has been found that the distribution of the z-component of the Poynting vector under the particles in the x–y plane near the central maximum can be, quite often with a sufficient accuracy, approximated by a Gaussian function [**46**]

$$S(x, y) = S_0 \, \mathrm{e}^{-r^2/r_0^2} \tag{8}$$

where r is the radial coordinate and S_0 is the intensity enhancement factor.

Both $|E|^2$ and S_z intensity field distributions depend on the two key parameters of size parameter q defined as $q = 2\pi a/\lambda$ and particle refractive index. At small size parameter values less than π, the Mie scattering effect dominates over the lens focusing effect. As a result, both the electric field and the Poynting vector field are not focused but only scattered. The maximum fields are not on the bottom side of the particles but on the sides of the particles. As the size parameter increases to several times of π, the lens focusing effect becomes dominant. As can be seen from Fig. 3, the super-resolution (i.e. focus sizes along the two cross directions x and y are both below the diffraction limit) in electric field focusing was only occurring at several particular sets of system parameters. These sets of parameters provide very valuable information for designing the nanoimaging processes. On the other hand, it is a little surprising to see that all the size parameter values within the range $\pi \leqslant q \leqslant 20\pi$ always generate super-resolution foci for laser nanofabrication (Fig. 3(b)). Meanwhile, it can be seen that super-resolution is more likely to be obtained in the small size parameter range, especially when it is smaller than 20.

3.2 Particles on the surface

3.2.1 *Influence of the substrate on near-field optical enhancement*

With the extensions to the BV theory as in section 2.1, exact calculation of optical near-fields for a particle on the surface is possible. A computer program incorporating the aforementioned BV theory was developed in the present authors' group. As to non-polarized laser light, the final near-field intensity field $I = S_z$ could be considered as the total of the intensity fields calculated for the polarization angles of 0° (half-intensity p-polarized component) and 90° (half-intensity s-polarized component).

In spite of the difficulties in numerical calculation, the situation is rather clear from the physical point of view. Qualitatively the substrate surface works like a mirror coupled with a spherical resonator (particle); it should lead to an increase in optical enhancement S_0 and a decrease in the area of the field localization r_0 (sharpening effect). This effect is confirmed by calculations. In Fig. 4, the intensity distribution within the xz plane is shown for a polystyrene particle ($n = 1.6$ and $2a = 1.0$ μm) on the silicon surface under 248 nm laser irradiation. Gradations of the intensity are given from negative (dark) to positive (light) values. The dark area

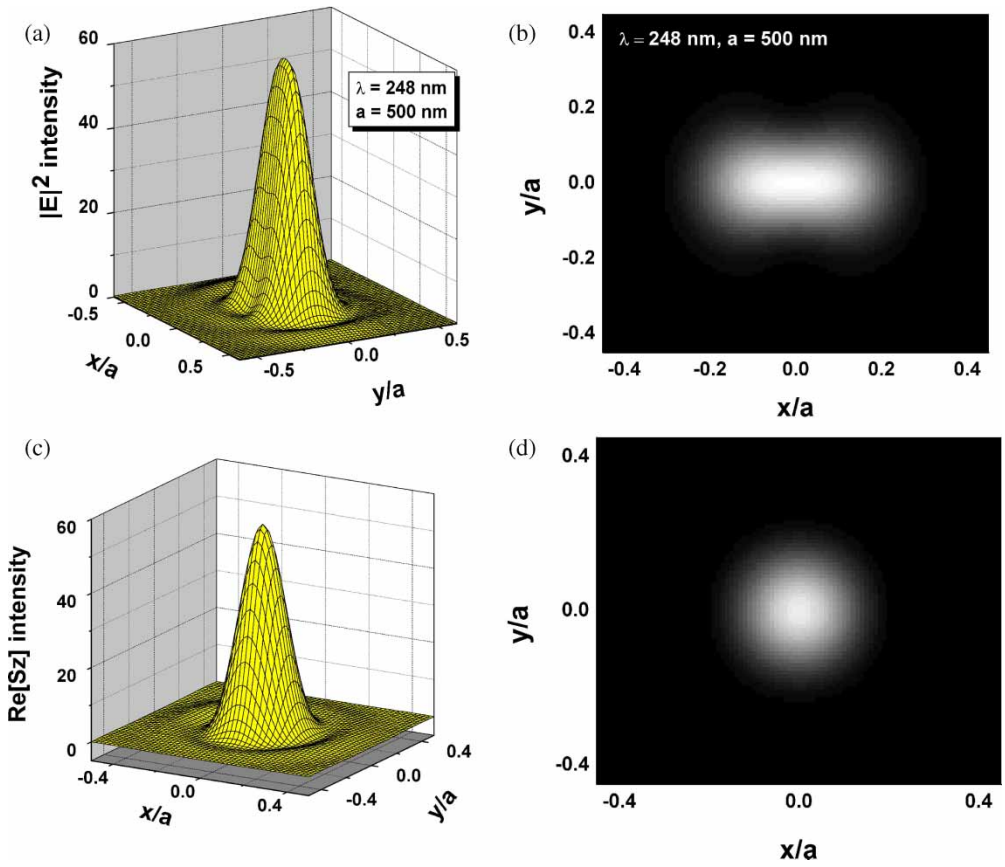

Fig. 2 Distribution of laser intensity within the tangential plane under the particles with radius $a = 0.5\,\mu$m, illuminated by a laser pulse at $\lambda = 248$ nm. (a) 3D picture of the $I = |E|^2$ intensity distribution, (b) contour plot of (a), (c) 3D picture of $I = S_z$ intensity distribution, and (d) contour plot of (c). The particle is considered to be non-absorbing ($\kappa = 0$) with refractive index $n = 1.6$

on the top of the particle corresponds to energy flux directed upward, while the white area under the particle corresponds to energy flux directed towards the substrate. From the figure, one can see enhanced radiation intensity, which passed through the transparent particle after its reflection by the surface. Compared with Mie results, the 'particle on surface' solution has several peculiarities.

First, it demonstrates a 1.5 times higher S_z intensity in the center than the Mie solution. Here, the solution was set by the present authors slightly below the substrate to see the absorbed radiation. This result was as expected, because the multi-reflection of the Poynting vector between the particle and the substrate results in more energy flowing into the substate. For a clear comparison, the results of calculations are summarized in Table 1. The following definitions are used:

(a) $X0$: full width at $1/e$ maximum in the x-direction (focusing size);
(b) $X1$: full width of the region with enhancement effect in the x-direction;
(c) $Y0$: full width at $1/e$ maximum in the y-direction (focusing size);
(d) $Y1$: full width of the region with enhancement effect in the x-direction;
(e) $\Delta d = X0 - Y0$ or $\Delta d = X1 - Y1$.

Second, the focusing intensity profile becomes sharper as $X0$ and $Y0$ both decrease ($X0$: 207 → 173 nm, $Y0$: 116 → 102 nm). The decrease of the Δd value (from 91 to 71 nm) indicates that the substrate has a 'homogenizer' effect on the electric field. For the S_z field, similar conclusions can be drawn from Table 1. This means that the near-field sharpening effect shown in the Mie solution will not diffuse because of secondary scattering. This result can be understood from the overall energy flux conservation within the range of the particle size.

3.3 Aggregated particles

In Mie and BV calculations, particles are in an isolated state and the field interactions between the neighbouring particles have been neglected. Here, the electromagnetic field distribution in monolayer particles with different aggregation states is simulated using the FIT technique. Figure 5 shows

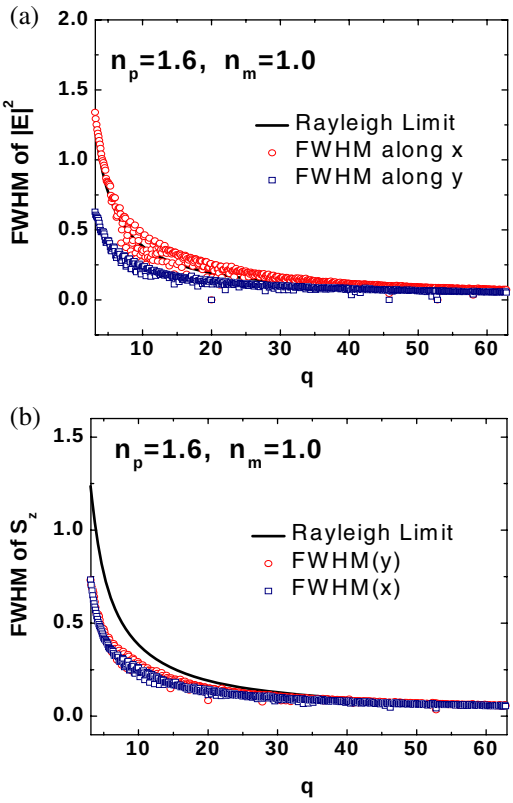

Fig. 3 Full width at half maximum (FWHM) of (a) $|E|^2$ focus and (b) $Re[S_z]$ focus sizes as a function of size parameter q defined as $q = 2\pi a/\lambda$, where a is the particle radius and λ is the laser wavelength. The particle is inside air or vacuum and assumed to be non-magnetic with a refractive index of 1.6. The FWHM values were normalized with respect to particle radius a

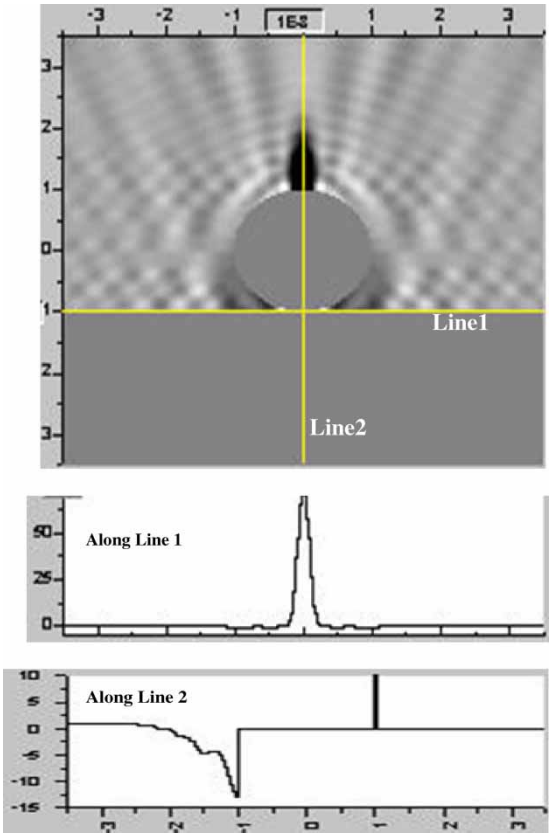

Fig. 4 The intensity $I = S_z$ distribution within the xz-plane for radiation with $\lambda = 248$ nm, scattered by a polystyrene particle ($n = 1.6$ and $a = 0.5\,\mu$m) on the Si surface. Gradations of the intensity are given from negative (dark) to positive (light) values. The dark area on the top of the particle corresponds to energy flux directed upward, while the white area under the particle corresponds to energy flux directed toward the substrate. Note that the field inside the particle is not calculated

the intensity field distribution, defined as the z-component of the Poynting vector $\boldsymbol{I} = S_z$, which represents the energy flowing into the substrate [**47**] when particles are arranged in different ways: (a) single particle, (b) three particles in a line, (c) seven particles in hexagonal form, and (d) an infinite number of particles in hexagonal form. It is observed that the field enhancement factor under the central particle (situated at $x = 0$ position) decreases with the number of particles surrounding it. The particles on the edge produce a higher intensity field underneath them, compared to the central particle in a line or to an isolated particle. When a particle has six surrounding particles as in Fig. 5(c), the field enhancement under the central particle is around 43, which is clearly below the enhancement of 54 for an isolated particle as in Fig. 5(a). By contrast, the particles at the edges give an enhancement of 60 that is higher than that of an isolated particle. The peak difference between the central and edged particles in this seven-particle system (Fig. 5(c)), reaches $\Delta I_{(\text{central-edge})} = 17$ (40 per cent decrease in percentage), which is higher than the peak difference in the three-sphere system (Fig. 5(b)), where $\Delta I_{(\text{central-edge})} = 4$ (8 per cent difference). For a perfect hexagonal array system, the enhancement under each particle is 34 (Fig. 5(d)), which is lower than the value of the central particle in the other three cases (Figs 5(a) to (c)). At the edge of a well-ordered hexagonal array, the peak difference between the central and edged particles was found to be $\Delta I_{(\text{central-edge})} \approx 20$ (60 per cent difference). Depending on these peak differences, one can expect some immediate effects that

Table 1 Comparison of near-field intensities calculated from Mie theory and BV theory

Intensity	Peak	$X0/X1$ (nm)	$Y0/Y1$ (nm)	$\Delta d = \lvert X_- - Y_- \rvert$ (nm)
$\lvert E\rvert^2$ (Mie)	59.59	207/328	116/224	91/104
$\lvert E\rvert^2$ (Substrate)	86.82	173/305	102/182	71/123
$\lvert S_z\rvert$ (Mie)	55.25	122/210	146/248	24/38
$\lvert S_z\rvert$ (Substrate)	72.19	123/228	119/198	4/30

have not been noticed by the PLA nanofabrication and laser cleaning community (i.e. the threshold for nanopatterning/laser cleaning could be very different for particles arranged in different forms). According to the findings given here, one can control the removal sequence of particles when laser fluence increases gradually from low to high values if the sample is processed by a single pulse. First, particles at the large array edge will be removed. This is followed by particles at the small array edge, isolated particles, and particles within the central region of the array. In the case where multiple laser pulses are used, the area of a particle array shrinks after each pulse due to the removal of particles at edges. New edges are formed after each pulse. The process can be repeated until the array has shrunk to a small number of particles. This can be explained by a process transition from the case of Figs 5(d) to (c), to (b), and finally to (a). By plotting the energy flow, it was found that there is a flow of energy from the central particles to edged particles.

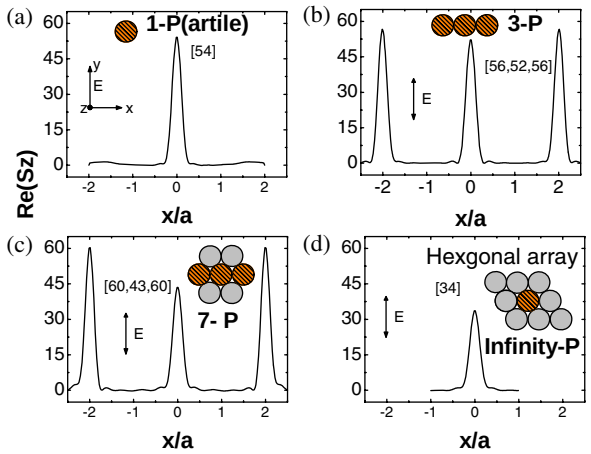

Fig. 5 Intensity field distribution under mono-layered particles arranged in different forms: (a) single particle, (b) three particles in a line, (c) seven particles in hexagonal form, and (d) an infinite number of particles in hexagonal form. The plot shows the z-component of the Poynting field distribution under the particles marked with line patterns

3.4 Particles inside water

To illustrate the basic physics of the focus tuning effect by a liquid medium, Mie theory modelling of an optical near field around a single particle has been carried out. Figure 6 shows the Mie modelling results of the cross-sectional view of the normalized local field distribution $|E|^2$ underneath a single 5.0 μm particle (a) in air and (b) immersed in water medium, under an x-polarized plane wave excitation at 800 nm. As can be seen in Fig. 6(a), the focus point of a 5.0 μm particle in air is located at position $z/a = 1.1$, which is close (subwavelength distance) to the particle surface. This means that for efficient surface patterning the sample must be kept in near-field contact with particles. As such, PLA tends to be removed after single pulse irradiation due to substrate thermal expansion or ablative force. On the other hand, the focusing properties of particles change dramatically when a surrounding medium is used. As can be seen from Fig. 6(b), the presence of water medium greatly extends the

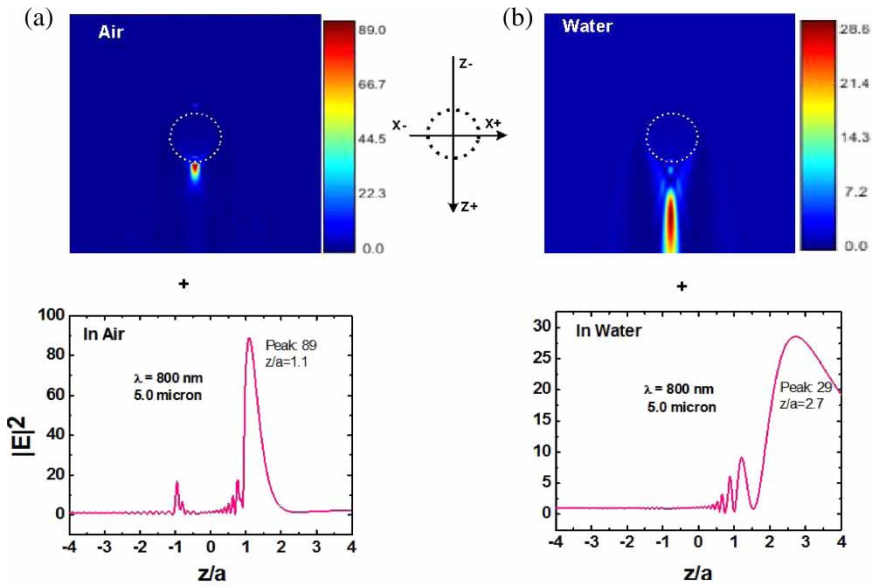

Fig. 6 Cross-sectional view of the normalized local field distribution ($|E|^2$) underneath a single 5.0 μm particle in (a) air and (b) immersed in water medium. The incident laser ($\lambda = 800$ nm) beam is linearly polarized along the x-axis and propagates along the z-axis

focal length, from $z/a = 1.1$ to $z/a = 2.7$, as compared to Fig. 6(a). In this case, PLA tends to remain on the surface after multiple laser shots. Meanwhile, the field enhancement decays from the focus point much slowly compared with that in Fig. 6(a) for air medium, resulting in a significant increase in the focus depth. It is beneficial for laser processing of materials in terms of fabricating higher-aspect-ratio structures into substrates with multiple shots, since more laser energy could be coupled into substrate when focus depth is extended. To further understand the field for an array of 5.0 μm particles on glass inside water, we go beyond Mie theory and use the FIT technique for the field analyses. The structure was represented with a unit cell combined with periodical boundary conditions within the substrate plane. The mesh density was set as $\lambda/10$. A plane wave was incident perpendicular to the sample surface, with an open boundary applied in this direction. Figure 7 shows the corresponding calculation results of cross-sectional views of normalized local field distribution $|E|^2$ underneath a hexagonal array of 5.0 μm particles deposited on quartz substrate (a) in air and (b) immersed in water. The incident beam has a wavelength of 800 nm and is polarized along the horizontal direction. Compared with the single particle case as in Fig. 6, it is found that the fields in Fig. 7 become oscillating while the focus point (highest enhancement peak) remains almost the same. Meanwhile, the amplitudes of the fields within the focus regions were generally smaller than those in Fig. 6. The appearance of the tail of the focus (see P2 in Fig. 7(a)) extends the focal length, which could increase energy coupling into the deeper substrate regime (this situation remains the same for water medium). As pointed out in the previous section, there is an outgoing energy flow from particles within the hexagonal array to those particles situated on the edges of the array, which results in the decrease of

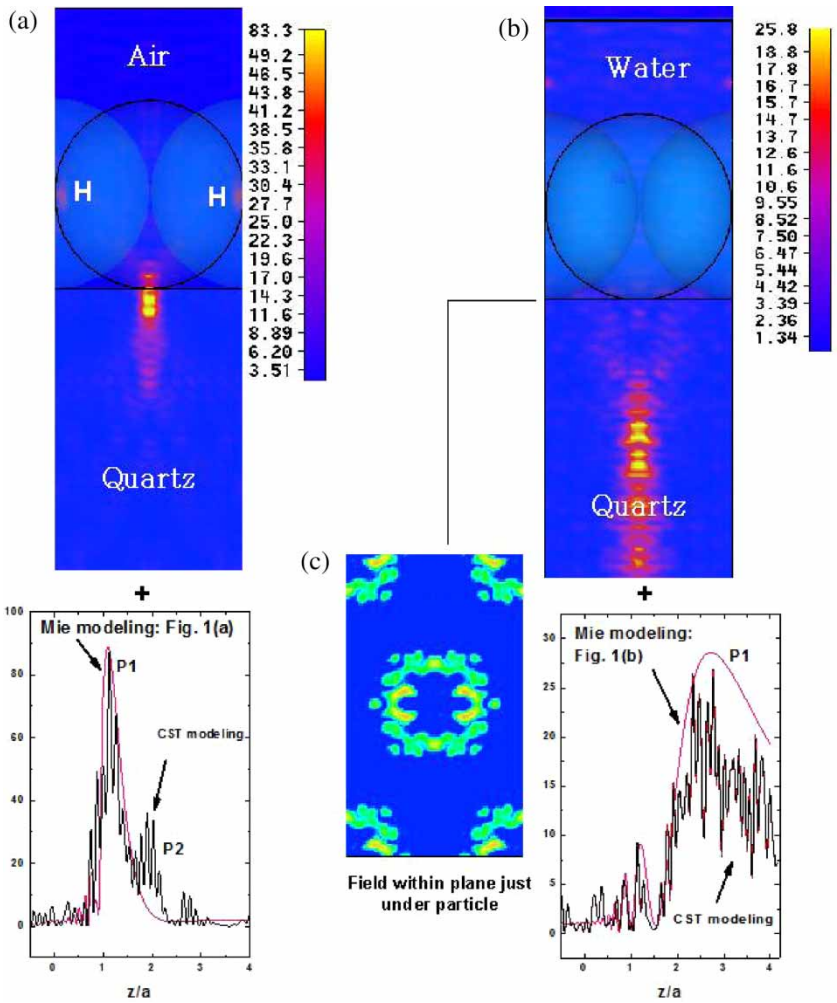

Fig. 7 Cross-sectional view of normalized local field distribution ($|E|^2$) underneath a hexagonal array of 5.0 μm particles deposited on the quartz substrate (a) in air and (b) immersed in water. The incident beam has a wavelength of 800 nm and is polarized along the horizontal direction. The refractive index of quartz and spheres are the same as 1.453 32 and 1.326 for water. (c) The electric field on substrate surface just under the particles

fields under the particles. This flow is clearly higher in air medium instead of water medium, as evidenced by the stronger coupling spots (marked as H-points) in Fig. 7(a). Multiple reflections of energy flows between the particles and the substrates could result in more laser energy flowing into the substrate. The final fields presented in Figs 7(a) and (b) could be thought of as the competing results of these two effects. In Fig. 7(c), it was shown that the electric field distribution on the substrate surface just beneath the particles manifests a ring-shaped profile.

3.5 Tip-sample system

This section looks at the optical near-field distributions in a tip-sample system, which were typically responsible for the laser nanofabrication with the combination of laser and AFM/STM-tip. Figure 8 shows the schematic of the tip-sample system studied here. The tip is modelled as a conical taper terminated by a hemisphere with a curvature diameter of $D2$, which typically ranges from 20 to 120 nm. The tip opening angle is 2α in the range from 10° to 40°. The tip-sample has a separation distance g of several nanometres. A plane wave, $\lambda = 532$ nm, is incident on the system at an oblique angle θ with respect to the tip-axis (z-axis). The incident wave is polarized so that the electric vector $\vec{E}$ lies in the xz plane. Four types of tip-sample systems were investigated and compared using the FIT technique: (a) a dielectric–dielectric system (silicon tip–silicon sample), (b) dielectric–plasmonic system (silicon tip–gold sample), (c) plasmonic–dielectric system (gold tip–silicon sample), and (d) plasmonic–plasmonic system (gold tip–gold sample). The dielectric objects were meshed at a density of $\lambda/10$, while the plasmonic objects were meshed at $\lambda/30$.

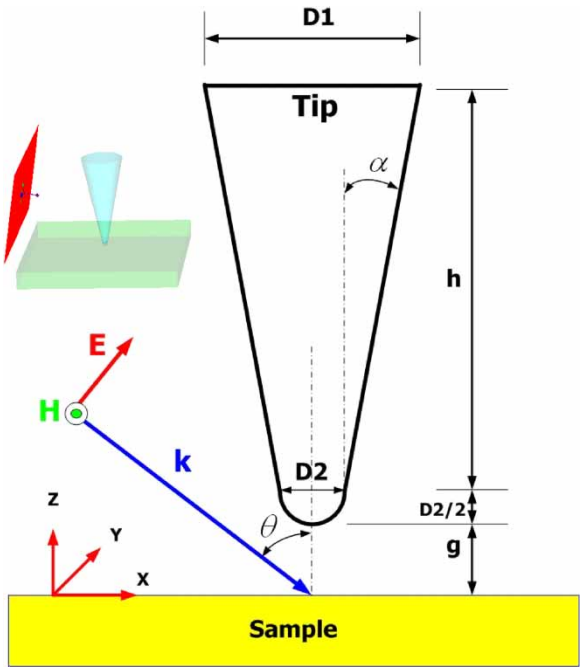

Fig. 8 Schematic of the tip-sample system simulated. The tip was modelled as a combination of a conical taper and a hemisphere of diameter $D2$. The opening angle of the tip is 2α. The relationship between $D1$ (diameter of the taper top), $D2$ (diameter of the taper bottom), and h (height of the taper) is given by $D1 = D2 + 2h\tan(\alpha)$. An electromagnetic plane wave of wavelength $\lambda = 532$ nm is incident at an angle θ with respect to the surface normal and is polarized in the xz-plane

Here, tip-sample geometry as in reference [**48**] is followed: $D2 = 70$ nm, $2\alpha = 25$, and $\theta = 80°$. The illumination length of the tip is ~25 μm. In the model, this illumination length was truncated to several micrometres due to the limited computational resources. The field distribution of the tip-sample system for different tip lengths ($h = 300$, 600, 1200, and 3000 nm) was calculated and compared. It is found that the field distribution in the tip-sample gap region is qualitatively the same for $h > \lambda$ (quantitatively, <8 per cent numerical difference between the results for $h = 600$ nm and $h = 3000$ nm), which is in agreement with reference [**49**]. As far as the field distribution within the gap region is concerned, the tip length of $h = 600$ nm is thus sufficient to provide a comprehensive representation of the field structure. Figure 9 shows the normalized $|E|^2$ intensity field distribution along the x-direction on the sample surface for the four tip-sample systems mentioned above. While keeping the laser incident angle fixed at 80°, the gap distance g was varied from 1 to 50 nm in the simulation. As can be seen in Fig. 9, the field maxima were reached at $g = 5$ nm for all the four systems, which is independent of the materials of the tip and sample. As g increases further, the intensity drops quickly. At $g \geqslant 20$ nm, almost no enhancement exists under the tip (for $g \geqslant 20$, all the cases are similar to Fig. 9(b)). Since the tip-sample systems reach their field maxima at the same gap distance regardless of the material, it could be suggested the dominant resonance modes excited in the gap region depend mainly on the geometry of the tip-sample system, e.g. the hemisphere diameter, tip opening angle, and incident angle. In the dielectric–dielectric and dielectric–plasmonic systems shown in Figs 9(a) and (b), two types of field profiles were observed: (a) double peak profiles with a central minimum for $g = 1$, 2 nm and (b) single peak profiles for $g \geqslant 3$ nm. The field in the dielectric–plasmonic gap region (Fig. 9(b)) is extremely sensitive when the tip-sample distance is within $2 \leqslant g \leqslant 3$ nm; a sudden increase of the field enhancement occurs for the 1 nm distance variation. In contrast, the field profiles in the plasmonic–dielectric and plasmonic–plasmonic systems at $g = 2$ nm and $g = 3$ nm are almost the same, as shown in Figs 9(c) and (d). Under

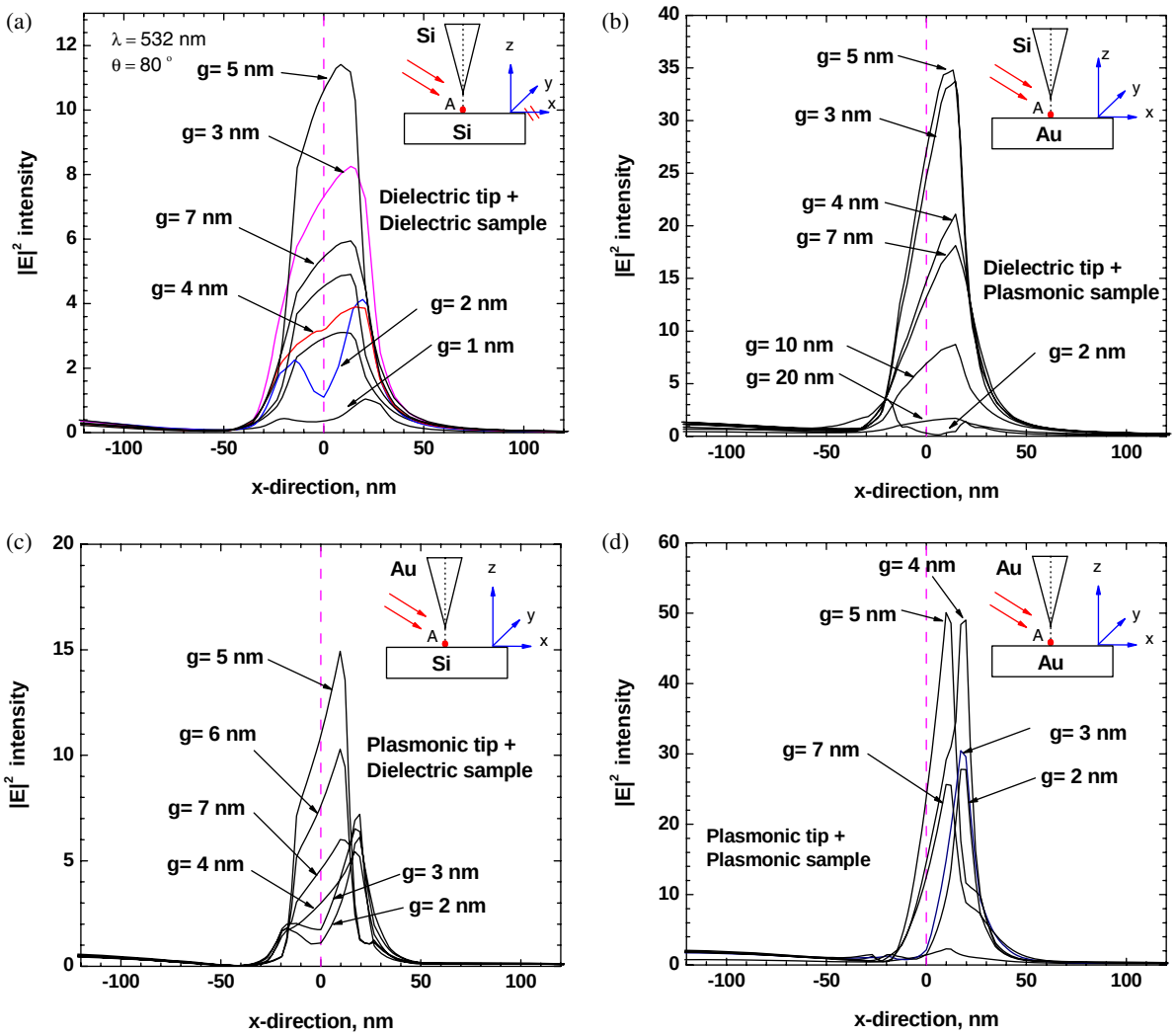

Fig. 9 Normalized $|E|^2$ intensity field distribution along the x-direction on the sample surface for four different tip-sample systems: (a) the dielectric tip + dielectric sample system, (b) the dielectric tip + plasmonic sample system, (c) plasmonic tip + dielectric sample, and (d) plasmonic tip + plasmonic sample. The incident angle is fixed at 80°

a typical STM tunnelling condition, the gap distance is ∼1 nm [**50**]. Owing to the fluctuation of experimental conditions as well as the tip-expansion/contraction effect under the pulsed laser illumination, the gap distance has a high probability of oscillating between 1 and 3 nm. Thus, the field sensitivity in a dielectric–plasmonic system could account for the observed chaotic behaviour of the tunnelling current in the nanosecond time scale [**50**]. Although the plasmonic material does not affect the geometrical resonance modes in the gap region, the plasmon resonance modes excited in the gold (Au) tip/sample (Figs 9(b) to (d)) at $\lambda = 532$ nm has increased the intensity of the field maxima as compared to the pure dielectric–dielectric system (Fig. 9(a)). An intensity peak of ∼50 can be seen in the plasmonic–plasmonic system in Fig. 9(d) at the position ($x = 10$ nm, $y = 0$ nm) on the surface when $g = 5$ nm. It is noted the peak position of the field maxima is not at the tip-sample 'contact' point ($x = 0$ nm, $y = 0$ nm, point A in the inset figures) but rather at a small distance δ ($5 \leqslant \delta \leqslant 20$ nm) away from the tip-axis in the x-direction. In a previous paper, we have shown the peak position shift effect for a 1.0 μm spherical particle situated on the sample surface, illuminated by an angular incident laser beam [**5**], both theoretically and experimentally. This effect, however, has not been reported so far in the literature for the experiments on nanopatterning by the laser-tip combination method. Two reasons could be given for this:

1. The shift distance $5 \leqslant \delta \leqslant 20$ nm could easily have been missed during AFM measurement.
2. The FE effect is not the dominant physical mechanism, and nanostructuring is instead caused by tip-sample mechanical contact as postulated by the thermal model.

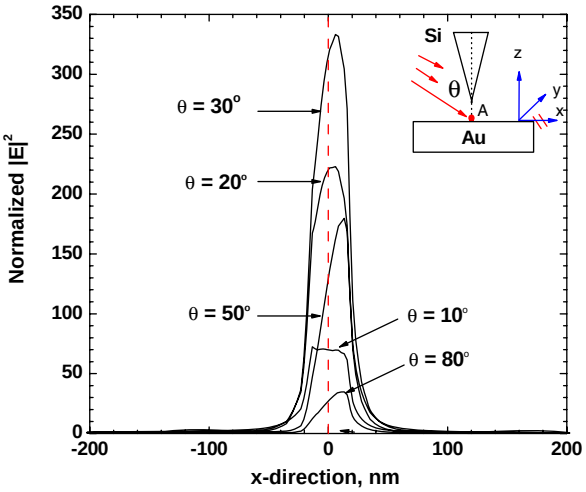

Fig. 10 Normalized $|E|^2$ intensity field distribution along the x-direction on the sample surface underneath the tip as a function of laser incident angle θ. The maximum intensity is about 333 at $\theta = 30°$

To identify the dominant mechanism, it is thus suggested that experimentalists in the field pay special attention to the location of nanofeatures relative to the position of a tip apex after processing; an experimental observation of the position shift could provide direct proof of the FE model.

In the experiments the laser incident angle θ was generally set as $>45°$ following the literature (e.g. 73° in reference [**51**], 80° in references [**48**] and [**50**], and 90° in reference [**52**]). The theoretical basis for doing so was established by Novotny *et al.* [**53**] who showed that it is crucial to have a large component of the excitation field along the axial direction (i.e. the vertical component E_z) to obtain a high field enhancement under the tip apex (the angle was set as 90° in their simulation [**53**]). It should be noted, however, the system studied by Novotny *et al.* contains only a tip and no substrate was taken into account. When a substrate is brought near to the tip, multiple reflections and scattering between them would take place and the field maximum was reached at some angle smaller than 90° [**54**] (i.e. the horizontal component of the excitation field E_x plays a more important role). Martin and Girard [**54**] reported an angle of 60° for the field maximum.

Figure 10 shows the intensity distribution on the sample surface as a function of the laser incident angle at a fixed gap distance of $g = 5$ nm, for the dielectric–plasmonic tip-sample system. All the parameters, except the incident angle θ, are the same as for Fig. 9(b). The angle was scanned in a range from 0° to 90° with a step size of 5°. It is found that the maximum intensity, ~333, occurs at $\theta = 30°$, which is much higher than the enhancement of ~35 at $\theta = 80°$. Calculations of the other three tip-sample systems (Figs 9(a), 8(c), and 8(d)) confirm that the angle of $\theta \approx 30°$ is the optimal angle for all the four tip-sample systems, regardless of the tip/sample material. It is important to note that at the angle $\theta \approx 30°$ the horizontal component of the excitation field E_x exceeds the vertical component E_z. Based on this effect, experiments studying the effects of variation of the incident angle could be designed and carried out to determine the dominating mechanism.

4 CONCLUSIONS

Theoretical methods and optical near-field distributions of different micro/nano-systems for PLA and laser-assisted AFM/STM-tip laser nanofabrication techniques are reviewed. It was noted that the field amplitude intensity is different from time-averaged intensity in the optical near-field. Spherical particles can effectively focus laser light for surface nanofabrication, with the strong ability to go beyond the diffraction limit. The presence of substrate increases field enhancement and homogenizes the focus. The coupling effect between neighbouring transparent particles tends to reduce the field enhancement factor by the particle. The focal length of the particle can be tuned by adding surrounding water so that nanofabrication of arrayed structures by PLA inside transparent glass is possible. For the conical tip-sample system, it has been found through modelling that the resonance mode excited in the tip-sample gap region is affected purely by the geometry and is independent of the material. The plasmon resonance helps to create a higher intensity in the optical near-field. We have identified two new effects in the conical tip-sample systems:

(1) The peak shift effect, where the intensity peak position is found to be shifted away from the shortest distance between the tip and sample.
(2) The dominance of the horizontal component of the incident wave over its vertical component.

These new effects can be utilized to design experiments to distinguish between the controversial mechanisms in the literature.

REFERENCES

1 **Novotny, L.** and **Hecht, B.** *Principles of nano-optics*, 2006 (Cambridge University Press, Cambridge).
2 **Abbe, E.** Beitrage zur Theorie des Mikroskops und der mikroskopischen Wahrnehmung. *Archiv Microskop. Anat.*, 1873, **9**, 413.
3 **Wang, Z. B., Luk'yanchuk, B. S., Hong, M. H., Lin, Y.,** and **Chong, T. C.** Energy flow around a small particle investigated by classical Mie theory. *Phys. Rev. B*, 2004, **70**, 035418.

4 **Huang, S. M., Hong, M. H., Lukiyanchuk, B.,** and **Chong, T. C.** Nanostructures fabricated on metal surfaces assisted by laser with optical near-field effects. *Appl. Phys. A*, 2003, **77**(2), 293–295.

5 **Wang, Z. B., Hong, M. H., Luk'yanchuk, B. S., Lin, Y., Wang, Q. F.,** and **Chong, T. C.** Angle effect in laser nanopatterning with particle-mask. *J. Appl. Phys.*, 2004, **96**, 6845–6850.

6 **Guo, W., Wang, Z. B., Li, L., Whitehead, D. J., Luk'yanchuk, B. S.,** and **Liu, Z.** Near-field laser parallel nanofabrication of arbitrary-shaped patterns. *Appl. Phys. Lett.*, 2007, **90**, 243101.

7 **Guo, W., Wang, Z. B., Li, L., Liu, Z., Luk'yanchuk, B.,** and **Whitehead, D. J.** Chemical-assisted laser parallel nanostructuring of silicon in optical near fields. *Nanotechnology*, 2008, **19**, 455302.

8 **Huang, S. M., Hong, M. H., Luk'yanchuk, B. S., Zheng, Y. W., Song, W. D., Lu, Y. F.,** and **Chong, T. C.** Pulsed laser-assisted surface structuring with optical near-field enhanced effects. *J. Appl. Phys.*, 2002, **92**(5), 2495–2500.

9 **Boneberg, J., Münzer, H.-J., Tresp, M., Ochmann, M.,** and **Leiderer, P.** The mechanism of nanostructuring upon nanosecond laser irradiation of a STM tip. *Appl. Phys. A*, 1998, **67**(4), 381–384.

10 **Dickmann, K., Jersch, J.,** and **Demming, F.** Focusing of laser radiation in the near-field of a tip (FOLANT) for applications in nanostructuring. *Surf. Interface Anal.*, 1997, **25**(7–8), 500–504.

11 **Jersch, J.** and **Dickmann, K.** Nanostructure fabrication using laser field enhancement in the near field of a scanning tunneling microscope tip. *App. Phys. Lett.*, 1996, **68**, 868.

12 **Lu, Y. F., Mai, Z. H., Zheng, Y. W.,** and **Song, W. D.** Nanostructure fabrication using pulsed lasers in combination with a scanning tunneling microscope: mechanism investigation. *Appl. Phys. Lett.*, 2000, **76**(9), 1200–1202.

13 **Betzig, E., Trautman, J. K., Wolfe, R., Gyorgy, E. M., Finn, P. L., Kryder, M. H.,** and **Change, C.-H.** Near field magneto-optics and high density data storage. *Appl. Phys. Lett.*, 1992, **61**(2), 142–144.

14 **Riehn, R., Charas, A., Morgado, J.,** and **Cacialli, F.** Near-field optical lithography of a conjugated polymer. *Appl. Phys. Lett.*, 2003, **82**(4), 526–528.

15 **Wysocki, G., Heitz, J.,** and **Bauerle, D.** Near-field optical nanopatterning of crystalline silicon. *Appl. Phys. Lett.*, 2004, **84**(12), 2025–2027.

16 **Lin, Y., Hong, M. H., Wang, W. J., Wang, Z. B., Chen, G. X., Xie, Q., Tan, L. S.,** and **Chong, T. C.** Surface nanostructuring by femtosecond laser irradiation through near-field scanning optical microscopy. *Sens. Actuators A, Phys.*, 2007, **133**(2), 311–316.

17 **Liu, Z., Wei, Q.,** and **Zhang, X.** Surface plasmon interference nanolithography. *Nano Lett.*, 2005, **5**(5), 957–961.

18 **Srituravanich, W., Durant, S., Lee, H., Sun, C.,** and **Zhang, X.** Deep subwavelength nanolithography using localized surface plasmons on planar silver mask. *J. Vac. Sci. Technol. B*, 2005, **23**(6), 2636–2639.

19 **Li, L. P., Lu, Y. F., Doerr, D. W.,** and **Alexander, D. R.** Laser-assisted nanopatterning of aluminium using particle-induced near-field optical enhancement and nanoimprinting. *Nanotechnology*, 2004, **15**(11), 1655–1660.

20 **Bouwkamp, C. J.** Diffraction theory. *Philips Rep. Phys.*, 1954, **27**, 35.

21 **Ohtsu, M.** and **Hori, H.** *Near-field nano-optics*, 1999 (Kluwer Academic, New York).

22 **Decca, R. S., Drew, H. D.,** and **Empson, K. L.** Investigation of the electric-field distribution at the subwavelength aperture of a near-field scanning optical microscope. *Appl. Phys. Lett.*, 1997, **70**(15), 1932–1934.

23 **Bethe, H. A.** Theory of diffraction by small holes. *Phys. Lett.*, 1944, **72**, 768.

24 **Courjon, D.** *Near field microscopy and near field optics*, 2003 (Imperial College Press, London).

25 **Paesler, M. A.** *Near-field optics: theory, instrumentation and applications*, 1996 (John Wiley Inc., New York).

26 **de Abajo, F. G.** Light transmission through a single cylindrical hole in a metallic film. *Opt. Express*, 2002, **10**, 1475–1484.

27 **Barnes, W. L., Dereux, A.,** and **Ebbesen, T. W.** Surface plasmon subwavelength optics. *Nature*, 2003, **424**(6950), 824–830.

28 **Ditlbacher, H., Krenn, J. R., Schider, G., Leitner, A.,** and **Aussenegg, F. R.** Two-dimensional optics with surface plasmon polaritons. *Appl. Phys. Lett.*, 2002, **81**(10), 1762–1764.

29 **Genet, C.** and **Ebbesen, T. W.** Light in tiny holes. *Nature*, 2007, **445**(7123), 39–46.

30 **Liu, Z. W., Steele, J. M., Srituravanich, W., Pikus, Y., Sun, C.,** and **Zhang, X.** Focusing surface plasmons with a plasmonic lens. *Nano Lett.*, 2005, **5**(9), 1726–1729.

31 **Martin-Moreno, L., Garcia-Vidal, F. J., Lezec, H. J., Pellerin, K. M., Thio, T., Pendry, J. B.,** and **Ebbesen, T. W.** Theory of extraordinary optical transmission through subwavelength hole arrays. *Phys. Rev. Lett.*, 2001, **86**(6), 1114–1117.

32 **Maier, S. A.** *Plasmonics: fundamentals and applications*, 2007 (Springer, New York).

33 **Stratton, J. A.** *Electromagnetic theory*, 1941 (McGraw-Hill, New York and London).

34 **Born, M.** and **Wolf, E.** *Principles of optics*, 1999 (Cambridge University Press, UK).

35 **Bobbert, P. A.** and **Vlieger, J.** Light scattering by a sphere on a substrate. *Physica*, 1986, **137A**, 209–242.

36 **Bobbert, P. A., Vlieger, J.,** and **Greef, R.** Light reflection from a substrate sparsely seeded with spheres – comparison with an ellipsometric experiment. *Physica*, 1986, **137A**, 243–257.

37 **Hafner, C.** *The generalized multiple multipole technique for computational electromagnetics*, 1990 (Artech, Boston).

38 **Lakhtakia, A.** Macroscopic theory of the coupled dipole approximation method. *J. Mod. Phys. C*, 1992, **3**, 583–603.

39 **Yang, W. H., Schatz, G. C.,** and **Vanduyne, R. P.** Discrete dipole approximation for calculating extinction and Raman intensities for small particles with arbitrary shapes. *J. Chem. Phys.*, 1995, **103**(3), 869–875.

40 **Martin, O. J. F., Girard, C.,** and **Dereux, A.** Generalized field propagator for electromagnetic scattering and light confinement. *Phys. Rev. Lett.*, 1995, **74**, 526.

41 **Jin, J. M.** *The finite element method in electromagnetics*, 2002 (John Wiley, New York).

42 Taflove, A. and **Hagness, S. C.** *Computational electrodynamics: the finite-difference time-domain method*, 3rd edition, 2005 (Artech House, Norwood).

43 Weiland, T. Time domain electromagnetic field computation with finite difference methods. *Int. J. Numer. Model.*, 1996, **9**, 295–319.

44 Rienen, U. V. *Numerical methods in computational electrodynamics; linear systems in practical applications*, 2001 (Springer, Berlin).

45 Computer Simulation Technology: CST Microwave Studio, 2007, available from http://www.cst.com.

46 Luk'yanchuk, B. S., Arnold, N., Huang, S. M., Wang, Z. B., and **Hong, M. H.** Three-dimensional effects in dry laser cleaning. *Appl. Phys. A*, 2003, **77**, 209–215.

47 Wang, Z. B., Hong, M. H., Luk'yanchuk, B. S., Huang, S. M., Wang, Q. F., Shi, L. P., and **Chong, T. C.** Parallel nanostructuring of GeSbTe film with particle-mask. *Appl. Phys. A.*, 2004, **79**, 1603–1606.

48 Huang, S. M., Hong, M. H., Lu, Y. F., Lukyanchuk, B. S., Song, W. D., and **Chong, T. C.** Pulsed-laser assisted nanopatterning of metallic layers combined with atomic force microscopy. *J. Appl. Phys.*, 2002, **91**, 3268.

49 Roth, R. M., Panoiu, N. C., Adams, M. M., Osgood Jr, R. M., Neacsu C. C., and **Raschke, M. B.** Resonant-plasmon field enhancement from asymmetrically illuminated conical metallic-probe tips. *Opt. Express*, 2006, **14**(7), 2921–2931.

50 Jersch, J., Demming, F., Fedotov, I., and **Dickmann, K.** Time-resolved current response of a nanosecond laser pulse illuminated STM tip. *Appl. Phys. A*, 1999, **68**(6), 637–641.

51 Kirsanov, A., Kiselev, A., Stepanov, A., and **Polushkin, N.** Femtosecond laser-induced nanofabrication in the near-field of atomic force microscope tip. *J. Appl. Phys.*, 2003, **94**(10), 6822–6826.

52 Lu, Y. F., Hu, B., Mai, Z. H., Wang, W. J., Chim, W. K., and **Chong, T. C.** Laser-scanning probe microscope based nanoprocessing of electronics materials. *Jpn. J. Appl. Phys.*, 2001, **40**, 4395.

53 Novotny, L., Bian, R. X., and **Xie, X. S.** Theory of nanometric optical tweezers. *Phys. Rev. Lett.*, 1997, **79**(4), 645–648.

54 Martin, O. J. F. and **Girard, C.** Controlling and tuning strong optical field gradients at a local probe microscope tip apex. *Appl. Phys. Lett.*, 1997, **70**, 705–707.